

## Supporting Information

### Atomic-level insights into the first cycle irreversible capacity loss of Ni-rich layered cathodes for Li-ion batteries

Anil K Paidi,<sup>†,¶</sup> Alex Taekyung Lee,<sup>‡,¶</sup> Vinod K Paidi,<sup>\*,¶</sup> Hyungju Ahn,<sup>†</sup> Jinsub Lim,<sup>§</sup> Kug-Seung Lee,<sup>†</sup> Sangsul

Lee,<sup>\*,†</sup> and Docheon Ahn<sup>\*,†</sup>

<sup>†</sup>*Pohang Accelerator Laboratory, POSTECH, Pohang-37673, Republic of Korea*

<sup>‡</sup>*Department of Applied Physics, Yale University, New Haven, Connecticut, 06511, United States*

<sup>¶</sup>*European Synchrotron Radiation Facility, 71 Avenue des Martyrs, Grenoble, 38043 Cedex 9, France*

<sup>§</sup>*Korea Institute of Industrial Technology (KITECH), 6, Cheomdan-gwagiro 208-gil, Buk-gu, Gwangju 61012, Republic of Korea*

*¶These authors contributed equally to this work*

**\*Corresponding Author:** paidi@esrf.fr; sangsul@postech.ac.kr; adc4055@postech.ac.kr

#### Keywords:

Li-ion batteries, Ni-rich cathodes, Synchrotron operando x-ray spectroscopy, Electronic structure, Irreversible capacity (IRC) loss, Capacity fading

## **Experimental Methods:**

### Synthesis of Materials

The spherical shaped  $[\text{Ni}_{0.90}\text{Co}_{0.05}\text{Mn}_{0.05}](\text{OH})_2$  precursor was synthesized by continuous type co-precipitation<sup>1</sup> method. The  $[\text{Ni}_{0.90}\text{Co}_{0.05}\text{Mn}_{0.05}](\text{OH})_2$  final precursor powder was obtained after washing with DI water, filtration, and drying at 110°C for 12 h. To obtain NCM900505, the dried final precursor was mixed with a Li source of LiOH exceeding 5 wt.% and then calcined at 750°C for 12 h, under oxygen flow.

### Scanning Electron Microscopy Experiments

Scanning electron microscopy (SEM) and EDS mapping of the NCM900505 powder was used to analyse the surface and morphology of the cathode samples using a High-resolution FE-SEM-II (JSM 7800F Prime with dual EDS).

### Operando X-ray Diffraction

The High-resolution synchrotron powder X-ray diffraction data (HRPD) of NCM900505 material was performed using synchrotron radiation at the Pohang Light Source (PLS-II) 9B-HRPD beamline. The incident X-rays were collimated by the mirror and monochromated to the wavelength ( $\lambda$ ) of 1.5219 Å via the double-crystal monochromator. A six multi-detector system was used with the analyzer crystal Ge(111) in the range of 15° to 135.5° with a step size of 0.01°. Operando XRD patterns were collected at 9A U-SAXS beamline with the X-ray wavelength ( $\lambda$ ) of 0.62586 Å of the incident beam and the sample-to-detector distance were calibrated using a LaB6 standard. For the operando small angle X-rays scattering (SAXS) measurements, a modified CR2032 coin-type half-cell with a pinhole diameter of 3 mm was constructed and the cell was charged and discharged at a 0.1 C rate within a voltage range from 2.7 V to 4.4 V using an 8-channel battery cycler (WonAtech).

The XRD patterns were continuously recorded every 3 min with a 2D charge-coupled device detector (Rayonix MX117-HS). For better evaluation, 2 $\theta$  angles for all the XRD patterns were

transformed to  $\lambda = 1.5406 \text{ \AA}$  (Cu K $\alpha$  radiation). The XRD patterns were integrated and analysed using FullProf Suite software.<sup>2</sup>

### Operando X-ray Spectroscopy

The X-ray absorption fine structure (XAFS) measurements of the Ni, Co, and Mn K-edges (1s $\rightarrow$ 4p) were performed under operando conditions at the beamline 8C of the Pohang Light Source-II. The X-ray beam from the undulator were monochromated by liquid nitrogen-cooled Si(111) double-crystal monochromator, where the beam intensity was reduced by 30% to eliminate the higher-order harmonics. The X-ray beam was then delivered to a secondary source aperture where the beam size was reduced to 0.5 mm (V)  $\times$  1 mm (H).

The obtained spectra were collected in both transmission and fluorescence modes. X-ray absorption near edge structure (XANES) and extended x-ray absorption fine structure (EXAFS) spectra were collected on continuous scans upon a fresh CR2032 coin-type half-cell with a 3 mm diameter pinhole positioned at a single-cell stage, during charge and discharge processes at 0.2 C-rate over a potential range between 2.7 and 4.4 V.

In the case of cathode material we have chosen i.e., NCM900505 and most of the similar Ni-rich Li[Ni<sub>x</sub>Co<sub>y</sub>Mn<sub>1-x-y</sub>]O<sub>2</sub> cathodes ( $x=0.6, 0.8, 0.9, \text{ and } 0.95$ ) the structural changes and phase transformations are within negligible changes between the uppercut off voltages 4.3 V and 4.4 V at a low C-rate as shown in Figure S2b.<sup>3,4</sup> Figure S2c illustrates the complete range of  $dQ/dV^{-1}$  curves for the NCM 900505 cathode at two different voltage ranges. We have matched each redox peak to the corresponding phase transition, and our findings align with previous literature<sup>5</sup> with a negligible change. We observed no substantial differences in electrochemical cycling between 4.3V and 4.4V charging, except for an enhanced capacity at 4.4V. (refer to Figures S2b and S2c). We employed an elevated voltage (higher SOC) range between 2.7 V – 4.4 V in our study and employing a marginally elevated potential allows for the efficient

extraction of electrons from Ni atoms, effectively capturing alterations in their oxidation state and electronic structure. For the Ni, Mn, and Co K-edge measurements, the energies were calibrated using Ni, Mn, and Co foils, respectively. EXAFS spectra were measured on Ni K-edge up to  $\sim 14 \text{ \AA}^{-1}$  in the wave vector  $k$  range to analyze the data.

On the other hand, for Mn and Co elements the spectra were only obtained up to  $\sim 10 \text{ \AA}^{-1}$  spectra were analysed using the ATHENA and ARTEMIS programs, an interface of IFEFFIT.<sup>6,7</sup> The empirical standards used for the XANES analysis are Ni foil,  $\text{Ni}_2\text{O}_3$ , NiO,  $\text{NiO}_2$ , Mn foil, MnO,  $\text{Mn}_2\text{O}_3$ ,  $\text{MnO}_2$ , Co foil,  $\text{Co}_3\text{O}_4$ , CoO, and  $\text{LiNiO}_2$ . The theoretical calculation of phase shifts and back scattering amplitudes for specific atom pairs were obtained using FEFF program.<sup>8</sup> Note that the overall reduction factor  $S_0^2$  was obtained by measuring and fitting foils.

Similarly, the normalized XANES spectra of the Mn K-edge spectra were compared with experimental standards (see Supporting Information, Figures S8 and S9). A comparison of the NCM900505 spectra with experimental references MnO (+2),  $\text{Mn}_2\text{O}_3$  (+3), and  $\text{MnO}_2$  (+4) show that the valence of Mn is of the order of +4. Interestingly, the Mn K-edge shifts to higher energies (Supporting Information, Figures S8) during charge/delithiation to 4.4 V, whereas, during lithiation/discharging to 2.7 V, no significant shift (Supporting Information, Figures S9) in the Mn K-edge indicates that Mn atoms do not contribute much to the charge compensation.

### Electrochemical Measurements

The electrochemical performance of the NCM900505 cathode material was examined using standard CR2032-type coin half-cells. The final electrodes were obtained by mixing the prepared cathode powders, conductive carbon (Super P, Timcal), and polyvinylidene fluoride (PVDF) binder (weight ratio of 90:5.5:4.5). N-methyl pyrrolidone (NMP) is the mixture solvent used, and the slurry was homogeneously mixed using a Fritsch mini mill (Pulverisette 23). The

mixed slurry was cast onto an Al current collector using a doctor blade, evenly and dried for 12 h at 120°C in a vacuum oven. The coated electrode with Al foil is roll pressed and punched into a wafer with a diameter of 14 mm with the average mass loading of all the cells was controlled at approximately ~2 mg. The 2032 coin-type half cells were assembled with the Li metal counter electrode, NCM900505 cathode, and a Celgard 2400 polypropylene porous membrane as separator in an Ar-filled glove box (Mbraun), maintaining an inert argon ambiance (H<sub>2</sub>O/O<sub>2</sub> level < 0.5 ppm). The electrolyte employed was 1 M LiPF<sub>6</sub> soluble in a mixture of ethylene carbonate (EC), ethyl methyl carbonate (EMC), and dimethyl carbonate (DMC) (volume ratio of 3:4:3) in 1 wt% Vinylene Carbonate (VC). The coin cells were cycled in a multi-channel battery analyzer (WBCS 3000, Wonatech, Korea). Galvanostatic charge/discharge measurements were carried out at ~C/5 rate within different potential ranges of cut-off voltages 2.7 V - 4.4 V (vs Li<sup>+</sup>/Li) at room temperature.

### Computational Methods

We employed the density functional theory (DFT) calculations using the projector augmented wave (PAW) method<sup>9</sup> and the revised version of the generalized gradient approximation (GGA) proposed by Perdew et al. (PBEsol),<sup>10</sup> as implemented in the VASP software.<sup>11</sup> The spin-dependent version of the exchange-correlation function is employed for all cases. A plane wave basis with a kinetic energy cutoff of 500 eV, and  $\Gamma$ - centered k-point meshes of size 8×8×5 were used.

We first considered 3×3×1 unit cells of LiNiO<sub>2</sub> (108 atoms) with H1 phase ( $R\bar{3}m$ , space group No. 166) and fully relaxed the lattice parameters. Atomic positions were relaxed until the residual forces were less than 0.01 eV/Å. We considered two different Li<sub>27</sub>Ni<sub>25</sub>Mn<sub>1</sub>Co<sub>1</sub>O<sub>54</sub> configurations (corresponds to Li<sub>1</sub>Ni<sub>0.93</sub>Mn<sub>0.04</sub>Co<sub>0.04</sub>O<sub>2</sub>), by randomly choosing two Ni atoms of LiNiO<sub>2</sub>, and replacing them with one Co and one Mn atom (See Figure S14). Next, we choose and remove three Li atoms randomly from each Li<sub>27</sub>Ni<sub>25</sub>Mn<sub>1</sub>Co<sub>1</sub>O<sub>54</sub> structure, and

considered four different configurations of  $\text{Li}_{24}\text{Ni}_{25}\text{Mn}_1\text{Co}_1\text{O}_{54}$  structures (corresponds to  $\text{Li}_{0.89}\text{Ni}_{0.93}\text{Mn}_{0.04}\text{Co}_{0.04}\text{O}_2$ ) (See Figure S14).

We used the GGA+U scheme within the rotationally invariant formalism together with the fully localized limit double-counting formula,<sup>12</sup> using  $U_d(\text{Ni})=3$  and  $U_d(\text{Co})=3$ , and  $U_d(\text{Mn})=3$ . While the magnetic ordering is not measured experimentally, we performed spin-polarized calculations and considered ferromagnetic order for all atomic configurations, since the high-spin state of the transition metal ion cannot be obtained by non-spin polarized calculations.<sup>13</sup> We also included van der Waals interaction,<sup>14</sup> but the effect of the van der Waals interaction on the lattice parameter is negligible up to 11% of Li vacancies, which is consistent with the study of other NCM materials.<sup>15</sup>

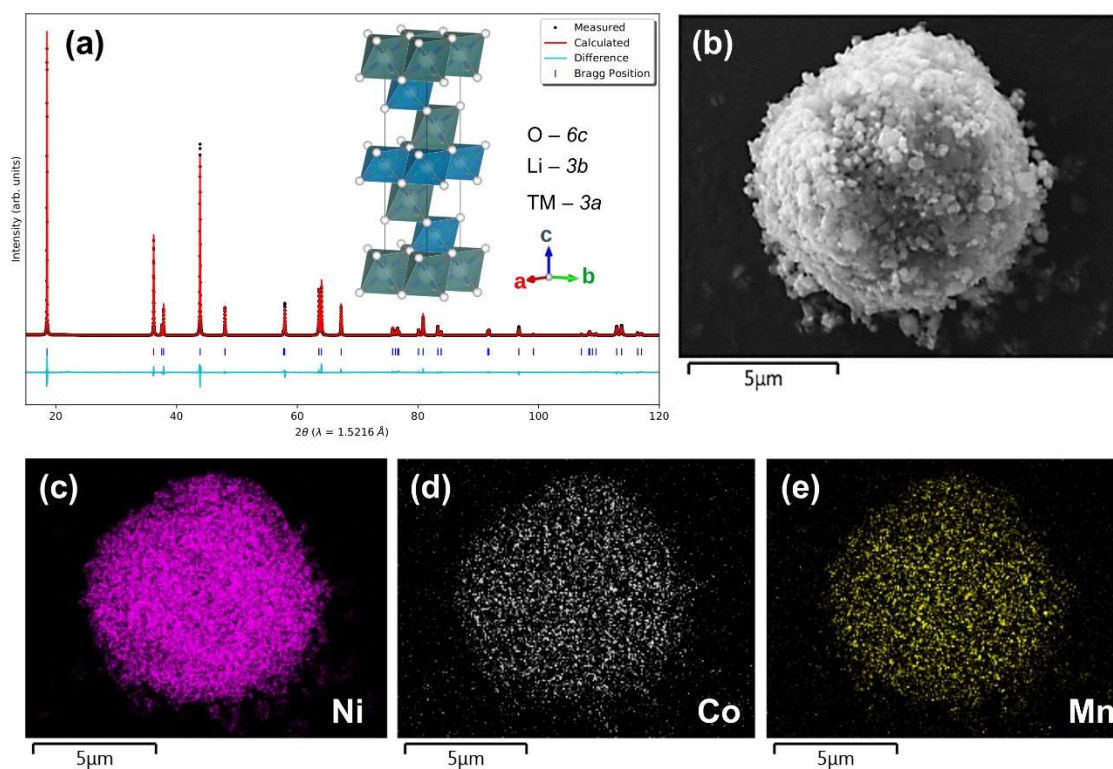


Figure S1. (a) Synchrotron powder diffraction pattern and Rietveld refinement of the NCM900505. The inset shows the unit cell of the layered structure. (b) SEM image and (c-e) EDX mapping of Ni, Mn, and Co show uniform transition metal distribution across the whole secondary particle.

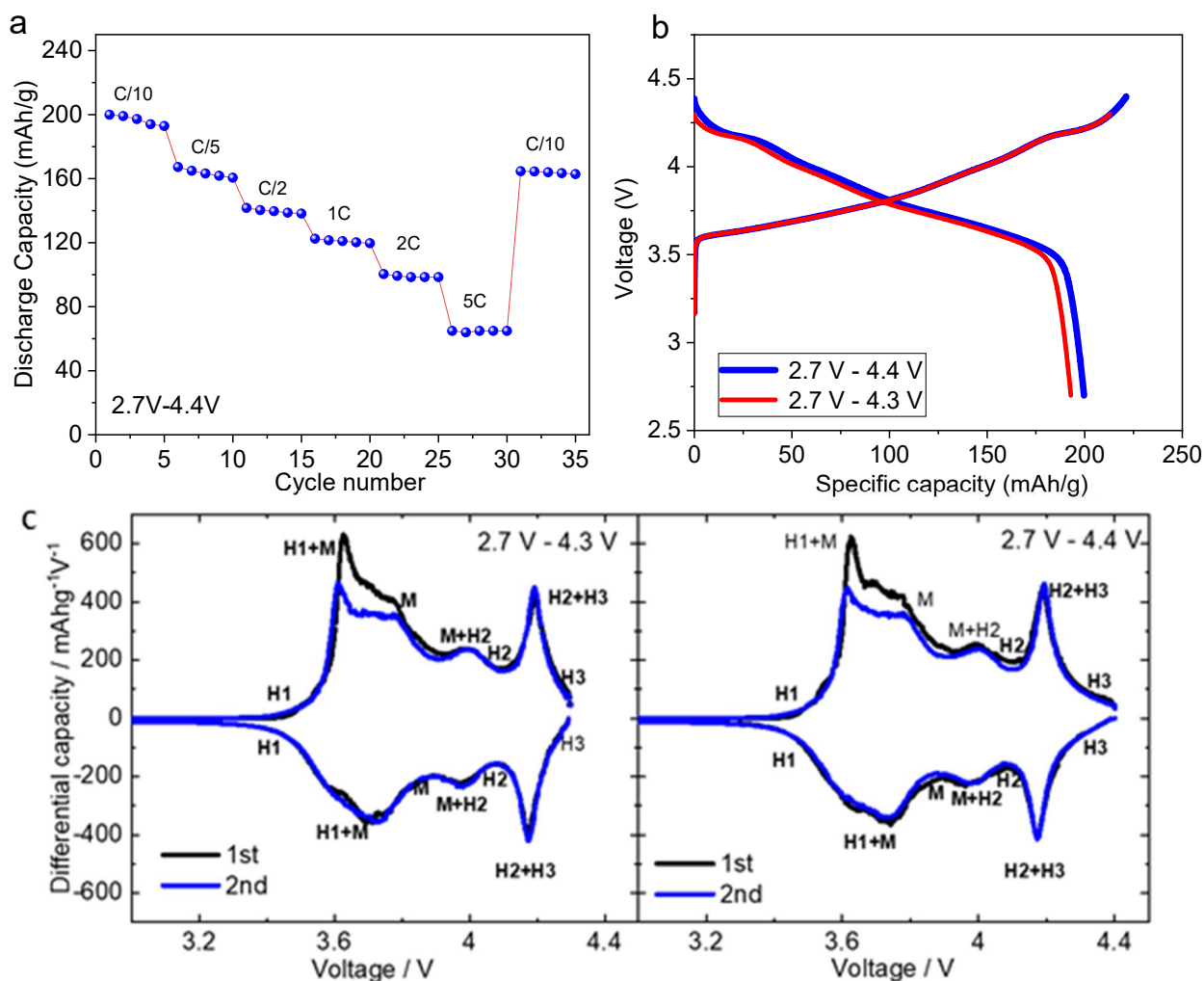


Figure S2. a) Rate test of NCM900505 cathode vs Li/Li<sup>+</sup> at a voltage range of 2.7 V – 4.4 V, b) Charge/discharge voltage profiles, c) dQ dV<sup>-1</sup> curves obtained by the first and second derivatives of the charge and discharge curves of NCM900505 at 2.7–4.3 V and 2.7–4.4 V.

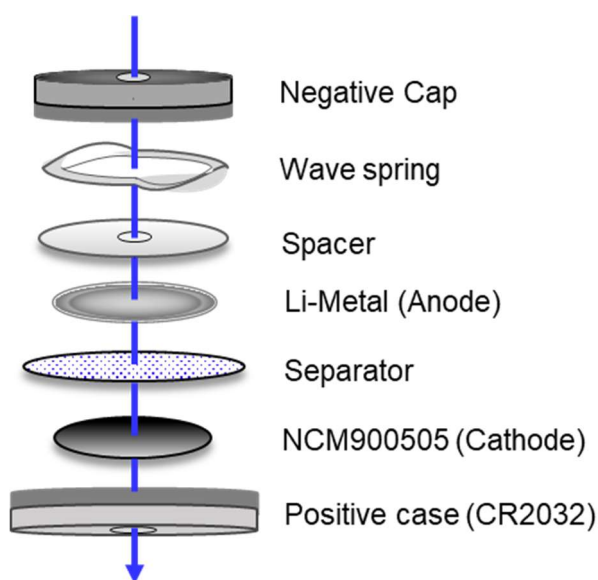


Figure S3. The schematic of the half-cell assembly of a CR2032 coin cell.

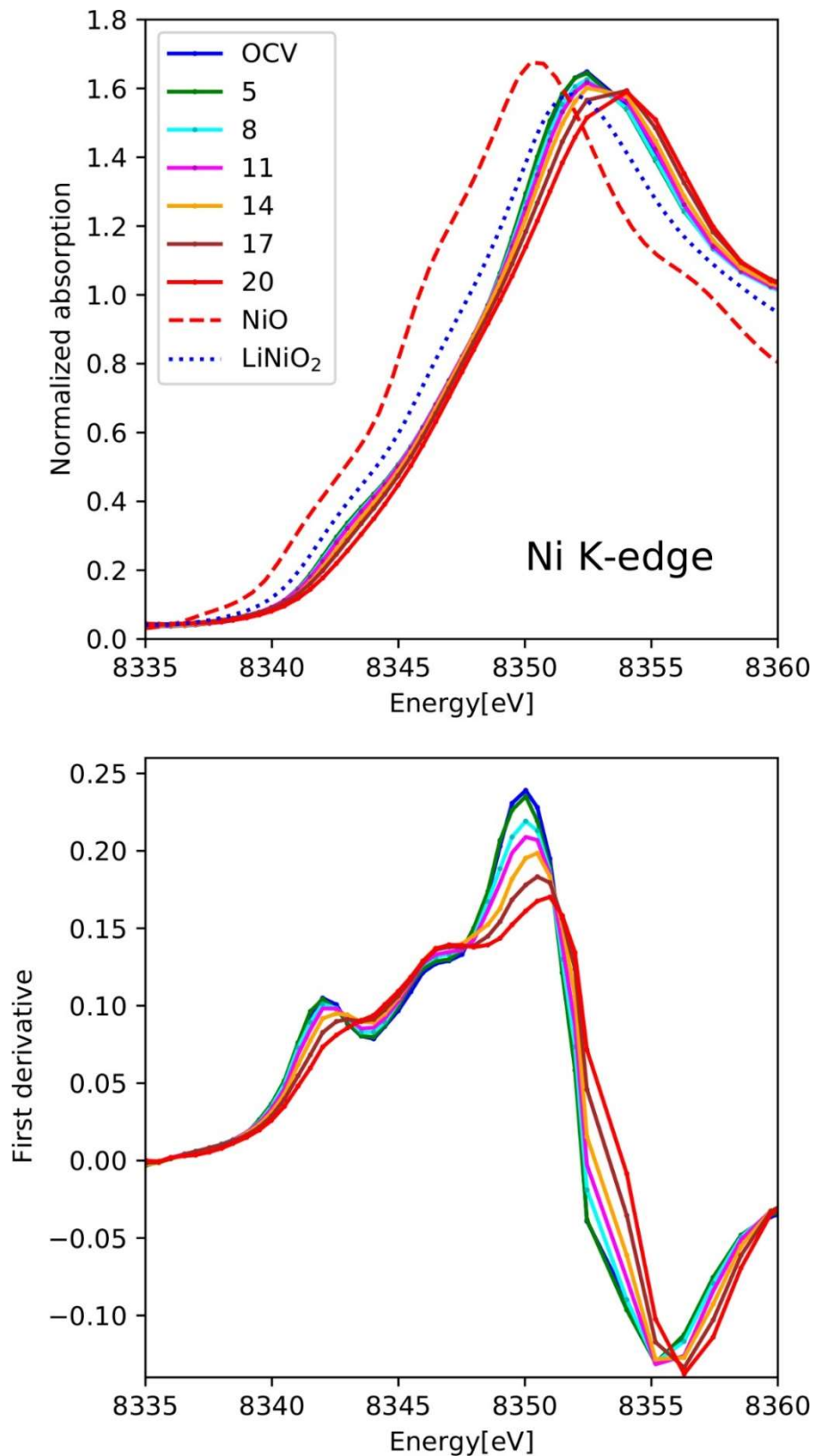


Figure S4. First-cycle Ni K-edge charging spectra of NCM900505 cathode. A comparison of the normalized XAS (top) and first derivative (bottom) spectra during charging. For clarity, the standards derivative spectra was not shown. Note that the OCV refers to open-circuit voltage, and numbers are indicative of spectrum numbers. With increase in time, the Ni K-edge shifts to the right.

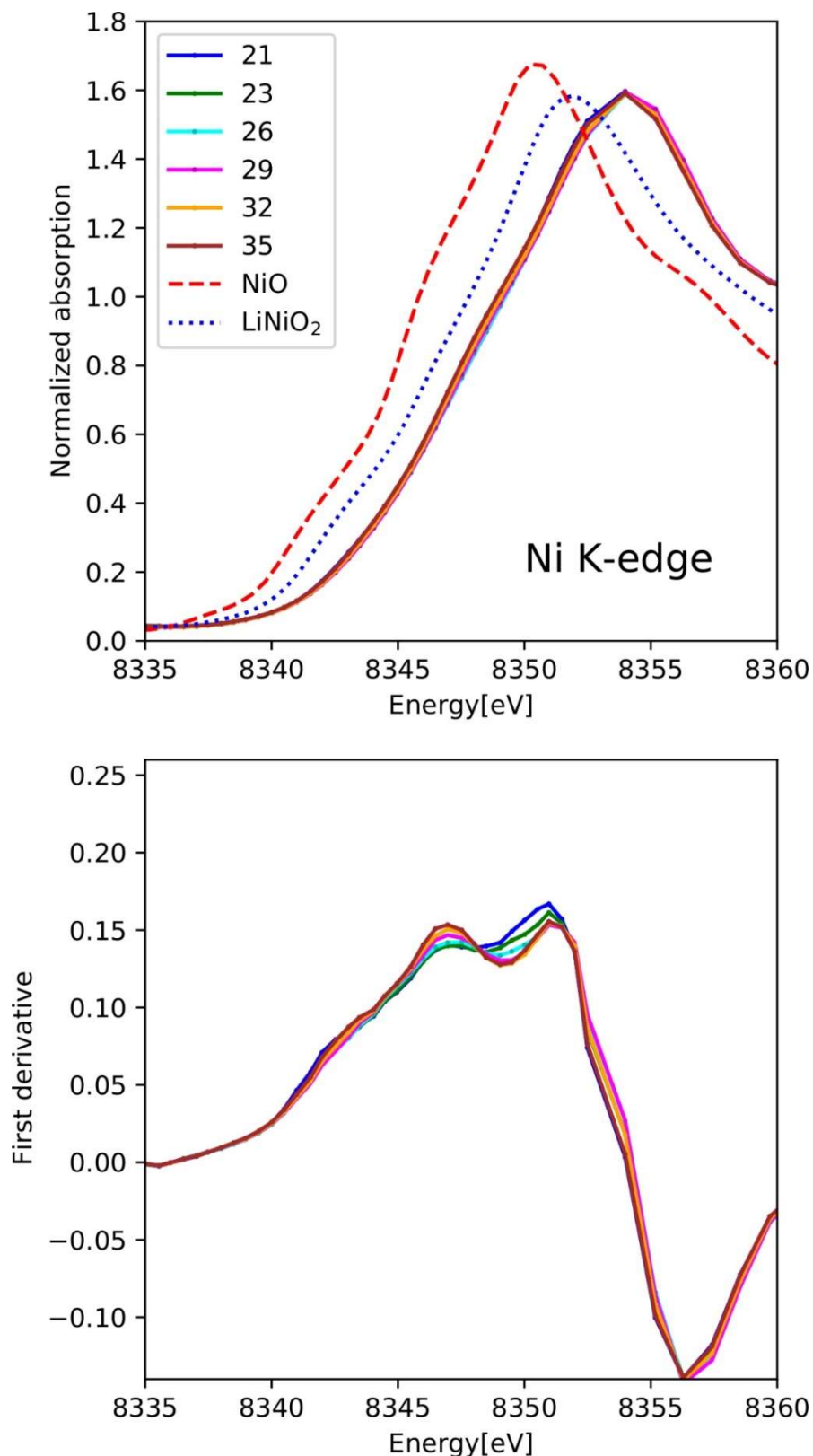


Figure S5. First-cycle Ni K-edge discharging spectra of NCM900505 cathode. A comparison of the normalized XAS (top) and first derivative (bottom) spectra during discharging. For clarity, the standards derivative spectra was not shown. Note that the OCV refers to open-circuit voltage, and numbers are indicative of the spectrum number. With discharging, the Ni K-edge do not fully retains its original position.

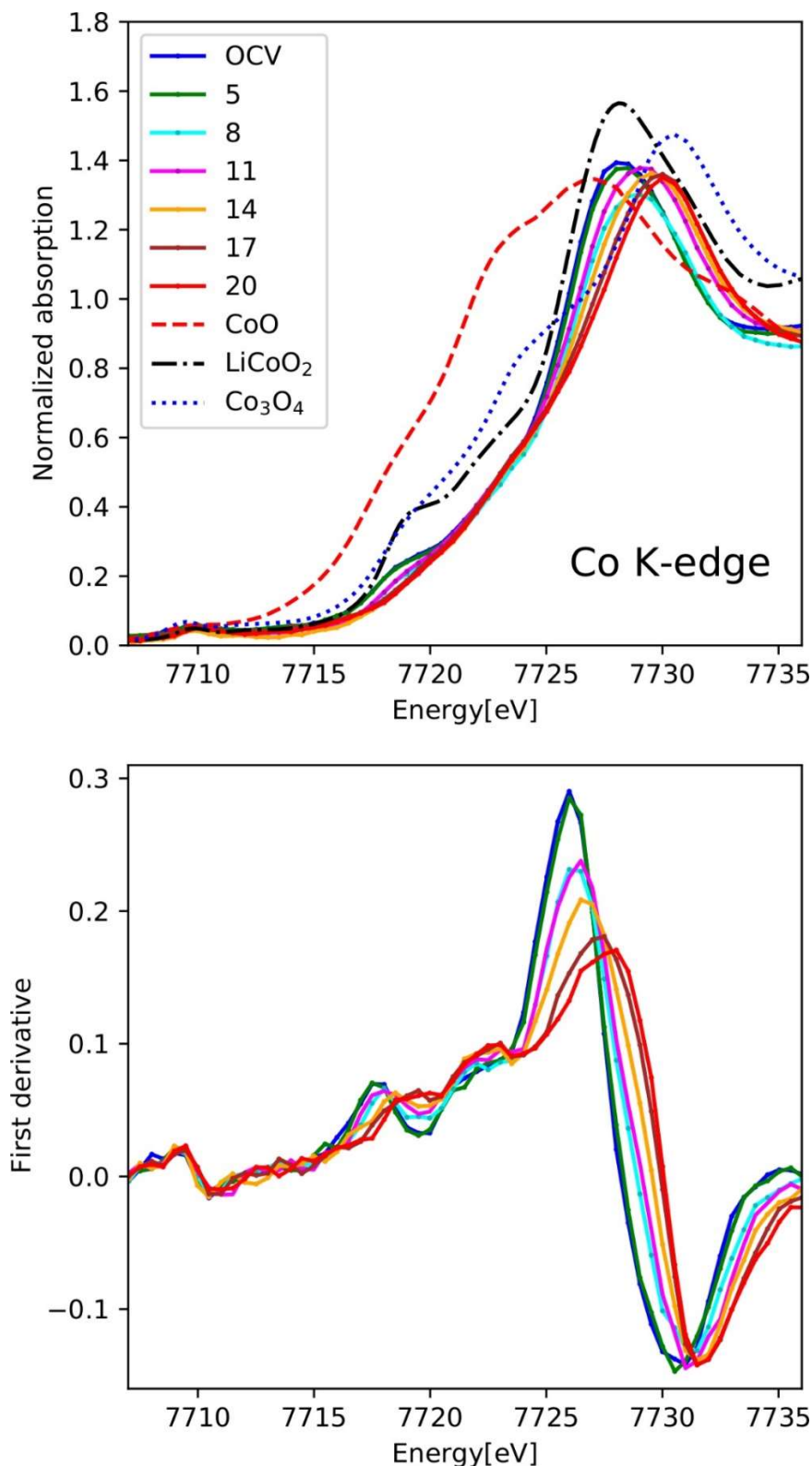


Figure S6. First-cycle Co K-edge charging spectra of NCM900505 cathode. A comparison of the normalized XAS (top) and first derivative (bottom) spectra during charging. For clarity, the standards derivative spectra was not shown. Note that the OCV refers to open-circuit voltage, and numbers are indicative of spectrum number. With increase in time, the Co K-edge shifts to the right.

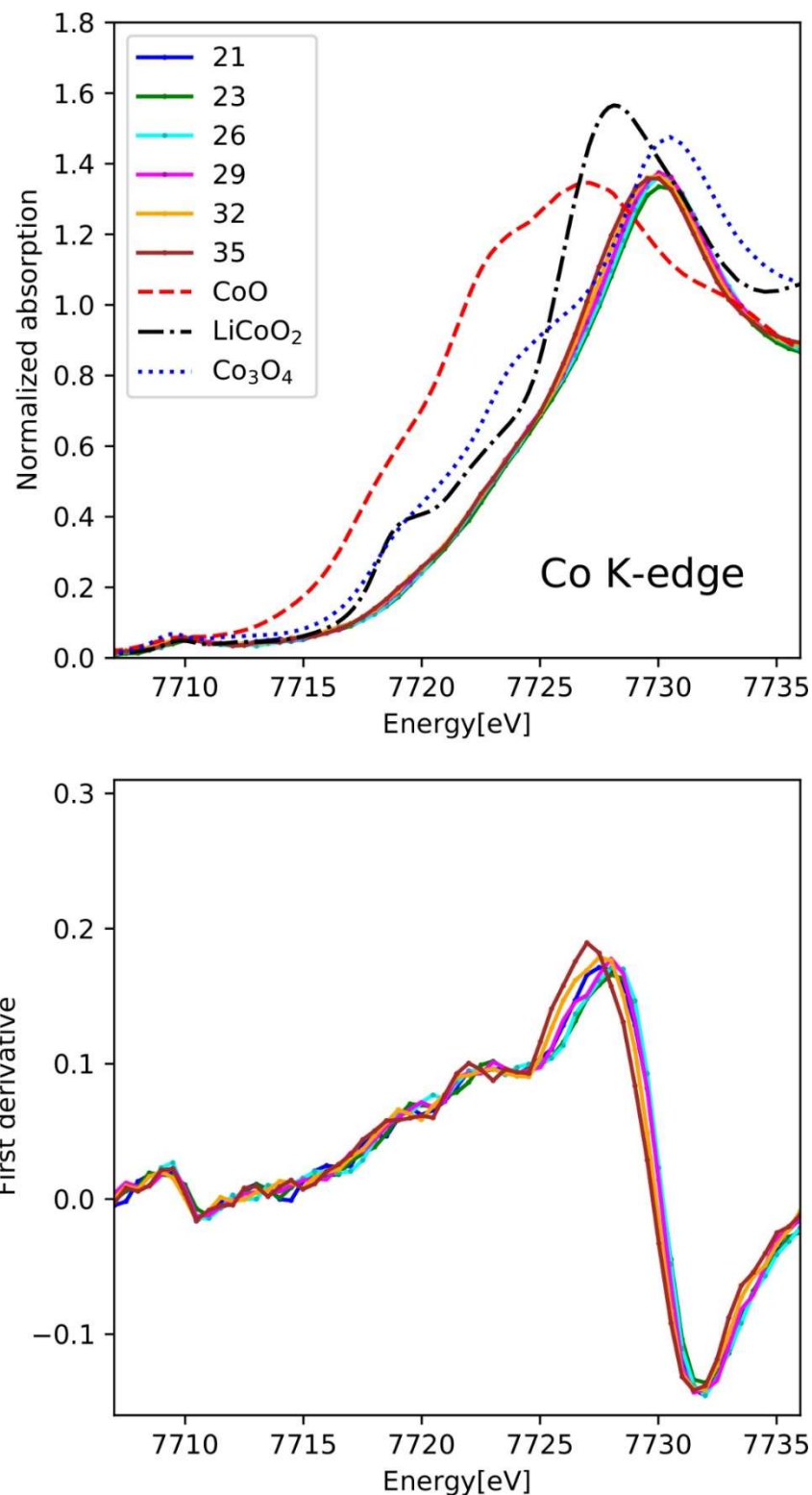


Figure S7. First-cycle Co K-edge discharging spectra of NCM900505 cathode. A comparison of the normalized XAS (top) and first derivative (bottom) spectra during discharging. For clarity, the standards derivative spectra was not shown. Note that the OCV refers to open-circuit voltage, and numbers are indicative of the spectrum number. With discharging, the Co K-edge do not fully retains its original position.

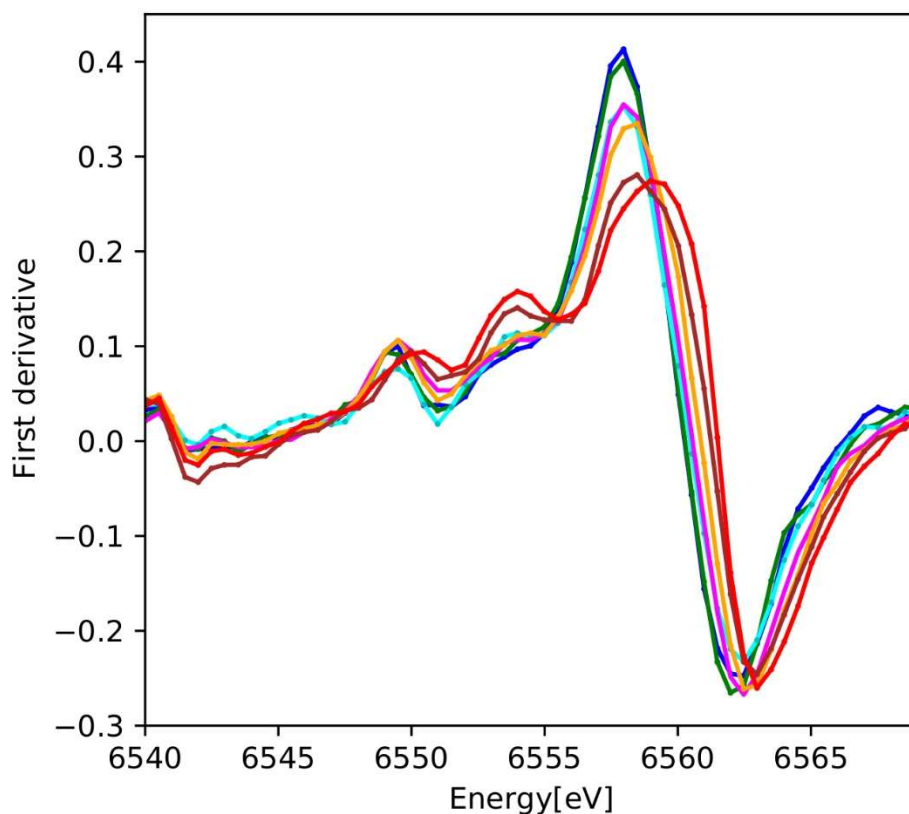
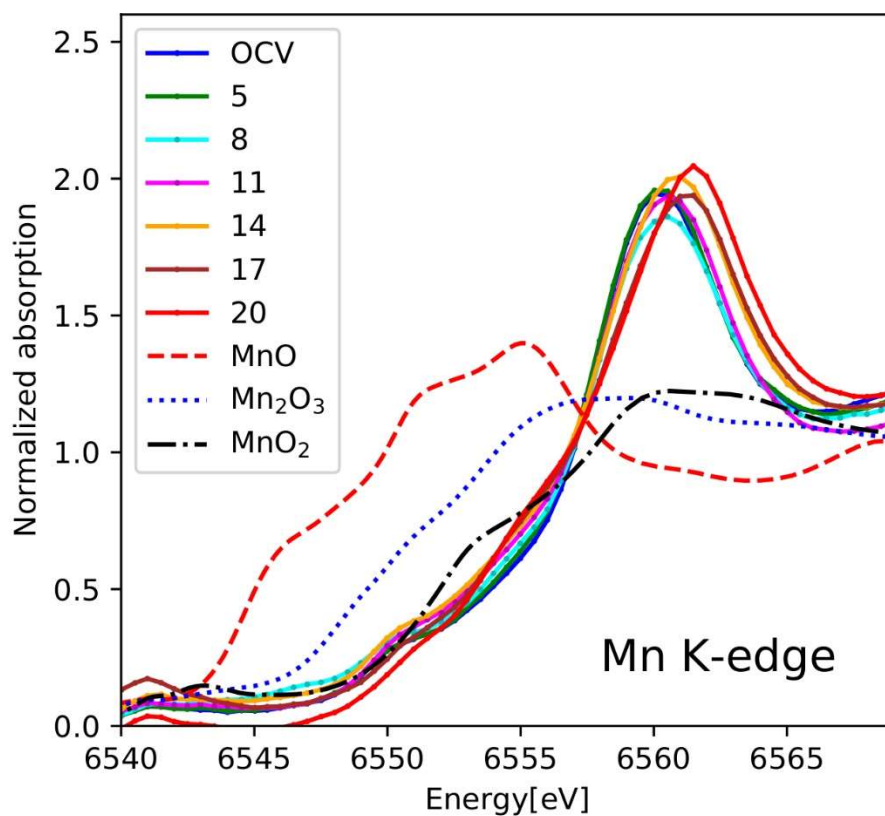


Figure S8. First-cycle Mn K-edge charging spectra of NCM900505 cathode. A comparison of the normalized XAS (top) and first derivative (bottom) spectra during charging. For clarity, the standards derivative spectra was not shown. Note that the OCV refers to open-circuit voltage, and numbers are indicative of spectrum number. With increase in time, the Mn K-edge shifts to the right.

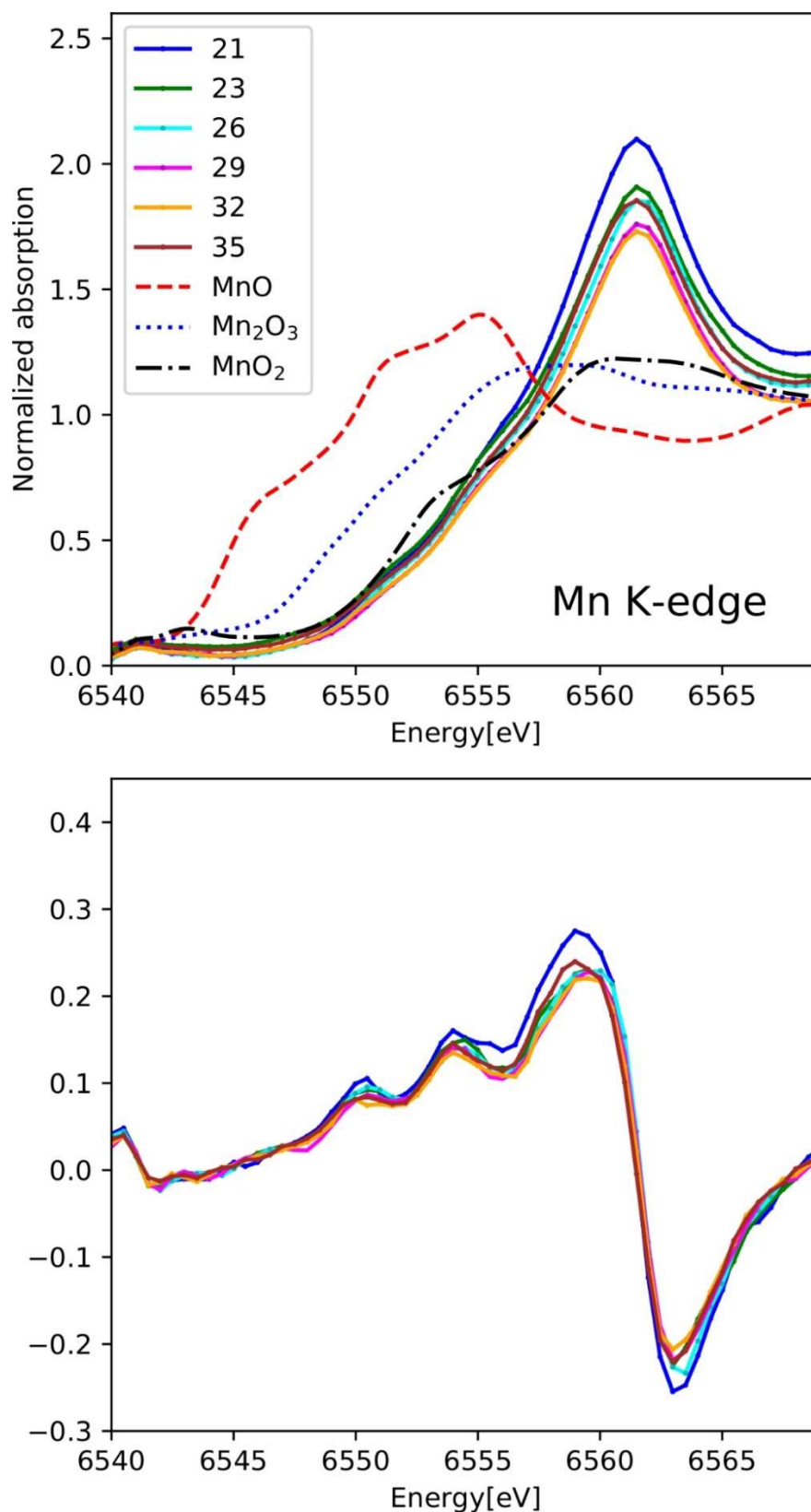


Figure S9. First-cycle Mn K-edge discharging spectra of NCM900505 cathode. A comparison of the normalized XAS (top) and first derivative (bottom) spectra during discharging. For clarity, the standards derivative spectra was not shown. Note that the OCV refers to open-circuit voltage, and numbers are indicative of the spectrum number. With discharging, the Mn K-edge do not fully retains its original position.

## EXAFS Charging Fits

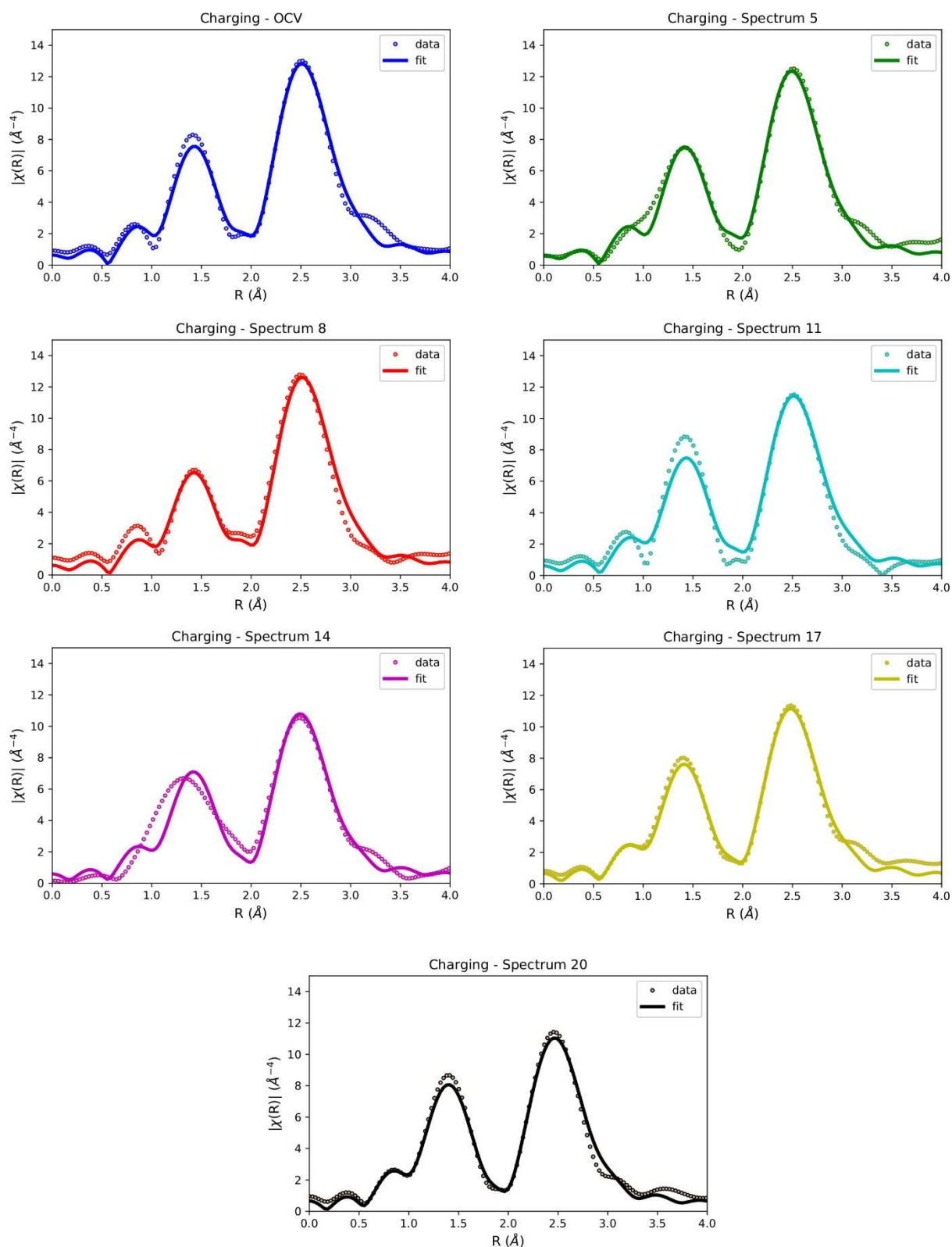


Figure S10. First-cycle Ni K-edge charging: The absolute Fourier transforms of the EXAFS spectra for the NCM900505 cathode. Circles and solid lines represent the experimental data and the theoretical fits, respectively.

## EXAFS Discharging Fits

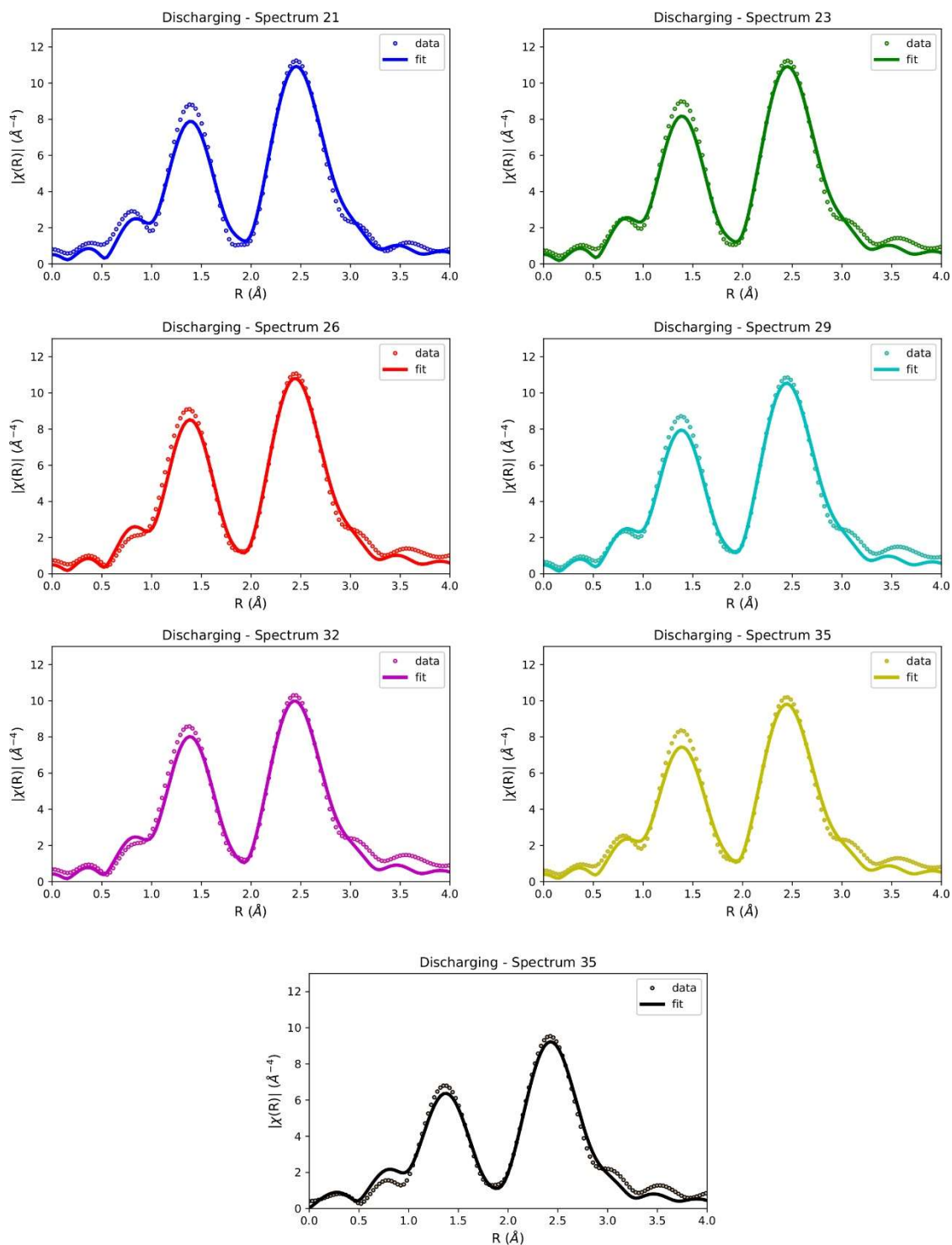


Figure S11. First-cycle Ni K-edge discharging: The absolute Fourier transforms of the EXAFS spectra for the NCM900505 cathode. Circles and solid lines represent the experimental data and the theoretical fits, respectively.

**Table S1. Fitting parameters of Ni K-edge ( $k^2$ -weighted) EXAFS spectra under operando conditions of NCM900505 cathode. Charging cycle.**

Spectrum Number <sup>a</sup>	shell	CN <sup>b</sup>	$R$ (Å) <sup>c</sup>	$\sigma^2$ ( $10^{-3}$ Å <sup>2</sup> ) <sup>d</sup>	$\Delta E_0$ (eV) <sup>e</sup>	$R$ factor
OCV	Ni–O	6	$1.96 \pm 0.01$	$10 \pm 1$	$-1.5 \pm 1.2$	0.007
	Ni–Ni	6	$2.89 \pm 0.01$	$5 \pm 1$		
5	Ni–O	6	$1.95 \pm 0.02$	$10 \pm 1$	$-2.1 \pm 1.4$	0.009
	Ni–Ni	6	$2.88 \pm 0.01$	$5 \pm 1$		
8	Ni–O	6	$1.96 \pm 0.02$	$12 \pm 2$	$-0.9 \pm 1.3$	0.008
	Ni–Ni	6	$2.89 \pm 0.01$	$5 \pm 1$		
11	Ni–O	6	$1.95 \pm 0.02$	$11 \pm 2$	$-1.5 \pm 1.8$	0.019
	Ni–Ni	6	$2.89 \pm 0.01$	$6 \pm 1$		
14	Ni–O	6	$1.94 \pm 0.02$	$11 \pm 2$	$-1.9 \pm 1.5$	0.016
	Ni–Ni	6	$2.88 \pm 0.01$	$7 \pm 1$		
17	Ni–O	6	$1.92 \pm 0.02$	$10 \pm 1$	$-2.2 \pm 1.0$	0.004
	Ni–Ni	6	$2.86 \pm 0.01$	$6 \pm 1$		
20	Ni–O	6	$1.91 \pm 0.01$	$10 \pm 1$	$-2.8 \pm 1.2$	0.007
	Ni–Ni	6	$2.85 \pm 0.01$	$7 \pm 1$		

<sup>a</sup>Spectrum number (see figure below to identify the region), <sup>b</sup>Coordination number (fixed value).

<sup>c</sup>Bond distance. <sup>d</sup>Debye–Waller factor. <sup>e</sup>Energy shift.

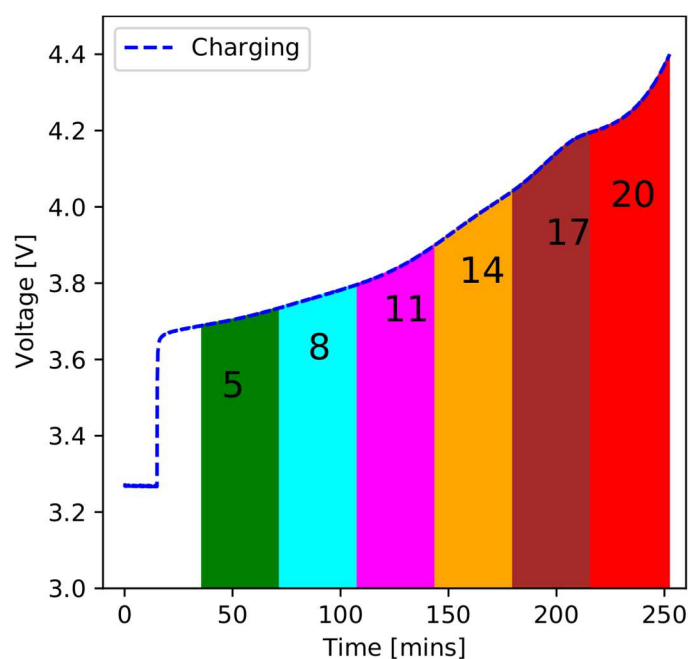
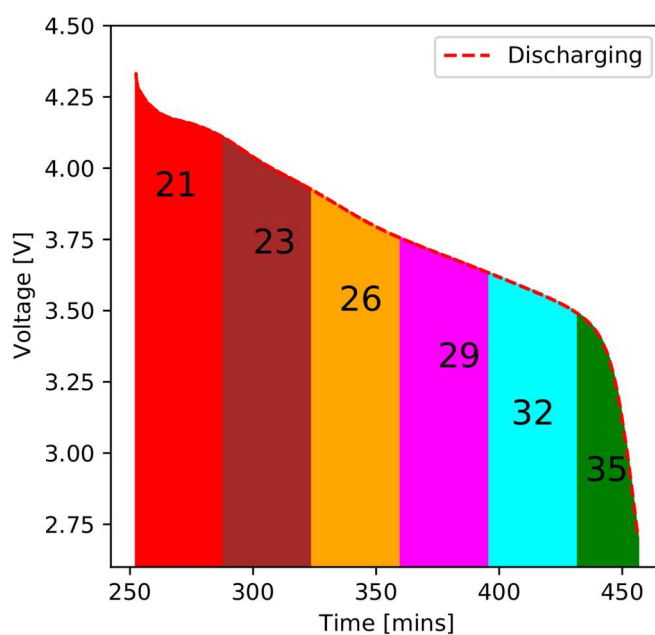


**Table S2. Fitting parameters of Ni K-edge ( $k^2$ -weighted) EXAFS spectra under operando conditions of NCM900505 cathode. Discharging cycle.**

Spectrum Number	shell	CN <sup>b</sup>	R (Å) <sup>c</sup>	$\sigma^2$ ( $10^{-3}$ Å <sup>2</sup> ) <sup>d</sup>	$\Delta E_0$ (eV) <sup>e</sup>	R factor
21	Ni–O	6	$1.91 \pm 0.02$	$10 \pm 1$	$-4.1 \pm 1.6$	0.012
	Ni–Ni	6	$2.85 \pm 0.01$	$7 \pm 1$		
23	Ni–O	6	$1.90 \pm 0.02$	$10 \pm 1$	$-4.2 \pm 1.6$	0.012
	Ni–Ni	6	$2.84 \pm 0.01$	$7 \pm 1$		
26	Ni–O	6	$1.90 \pm 0.01$	$9 \pm 2$	$-4.7 \pm 1.4$	0.009
	Ni–Ni	6	$2.84 \pm 0.01$	$7 \pm 1$		
29	Ni–O	6	$1.90 \pm 0.02$	$10 \pm 2$	$-4.4 \pm 1.5$	0.011
	Ni–Ni	6	$2.84 \pm 0.01$	$7 \pm 1$		
32	Ni–O	6	$1.90 \pm 0.02$	$9 \pm 1$	$-4.8 \pm 1.4$	0.001
	Ni–Ni	6	$2.84 \pm 0.01$	$7 \pm 1$		
35	Ni–O	6	$1.91 \pm 0.02$	$10 \pm 2$	$-4.6 \pm 1.7$	0.014
	Ni–Ni	6	$2.84 \pm 0.01$	$8 \pm 1$		
39	Ni–O	6	$1.91 \pm 0.01$	$11 \pm 1$	$-4.2 \pm 1.4$	0.010
	Ni–Ni	6	$2.85 \pm 0.01$	$7 \pm 1$		

<sup>a</sup>Spectrum number (see figure below to identify the region). <sup>b</sup>Coordination number (fixed value).

<sup>c</sup>Bond distance. <sup>d</sup>Debye–Waller factor. <sup>e</sup>Energy shift.



## Second-Cycle Ni K-Edge XANES

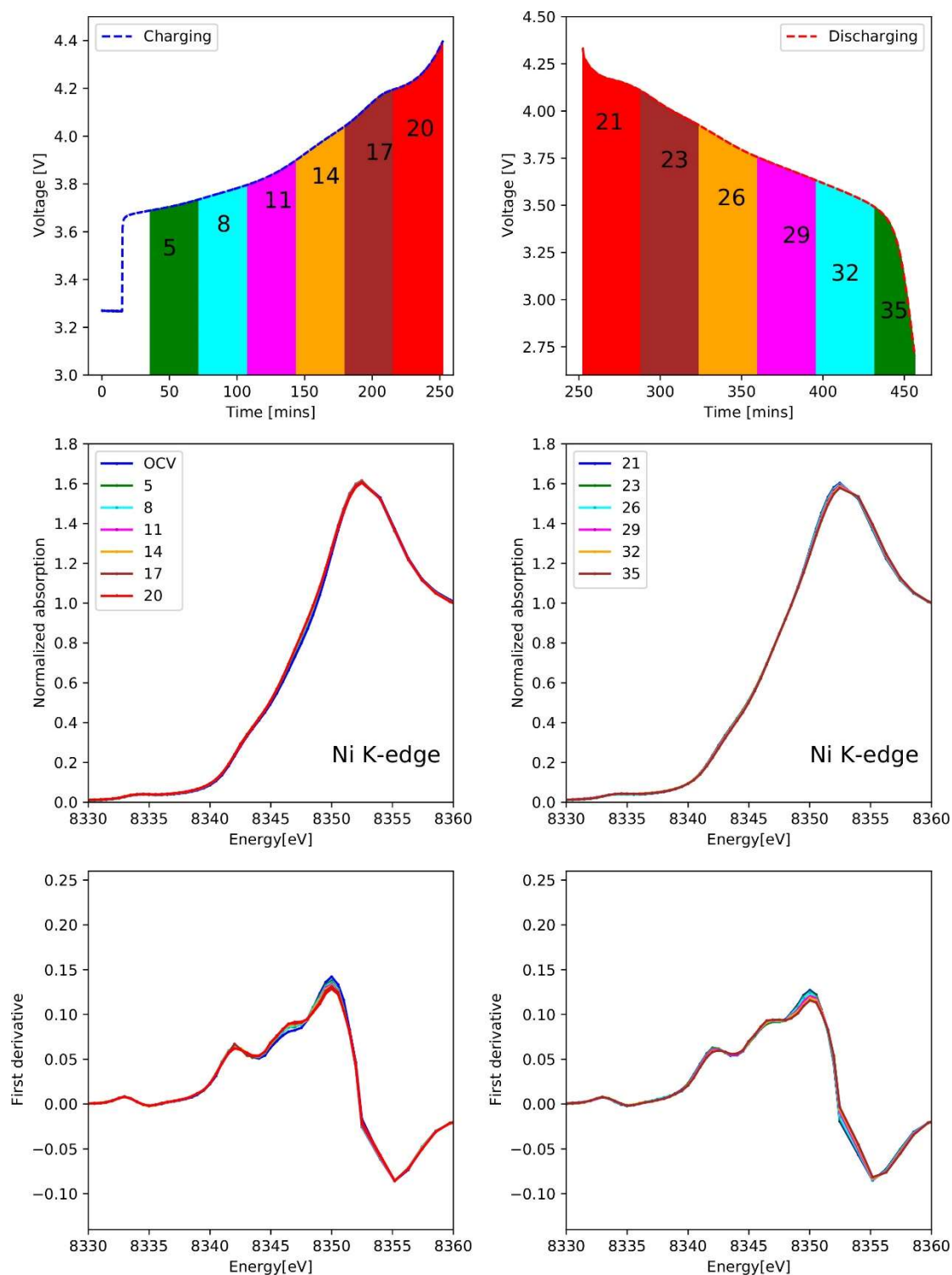


Figure S12. Second-cycle Ni K-edge charging spectra of NCM900505 cathode. A comparison of the normalized XAS (top) and first derivative (bottom) spectra during charging/discharging are shown. For clarity, the standards spectra was not shown. Note that the OCV refers to open-circuit voltage, and numbers are indicative of spectrum number. With charging/discharging, the Ni K-edge do not shifts to the higher/lower energies.

## Second-Cycle Ni K-Edge EXAFS

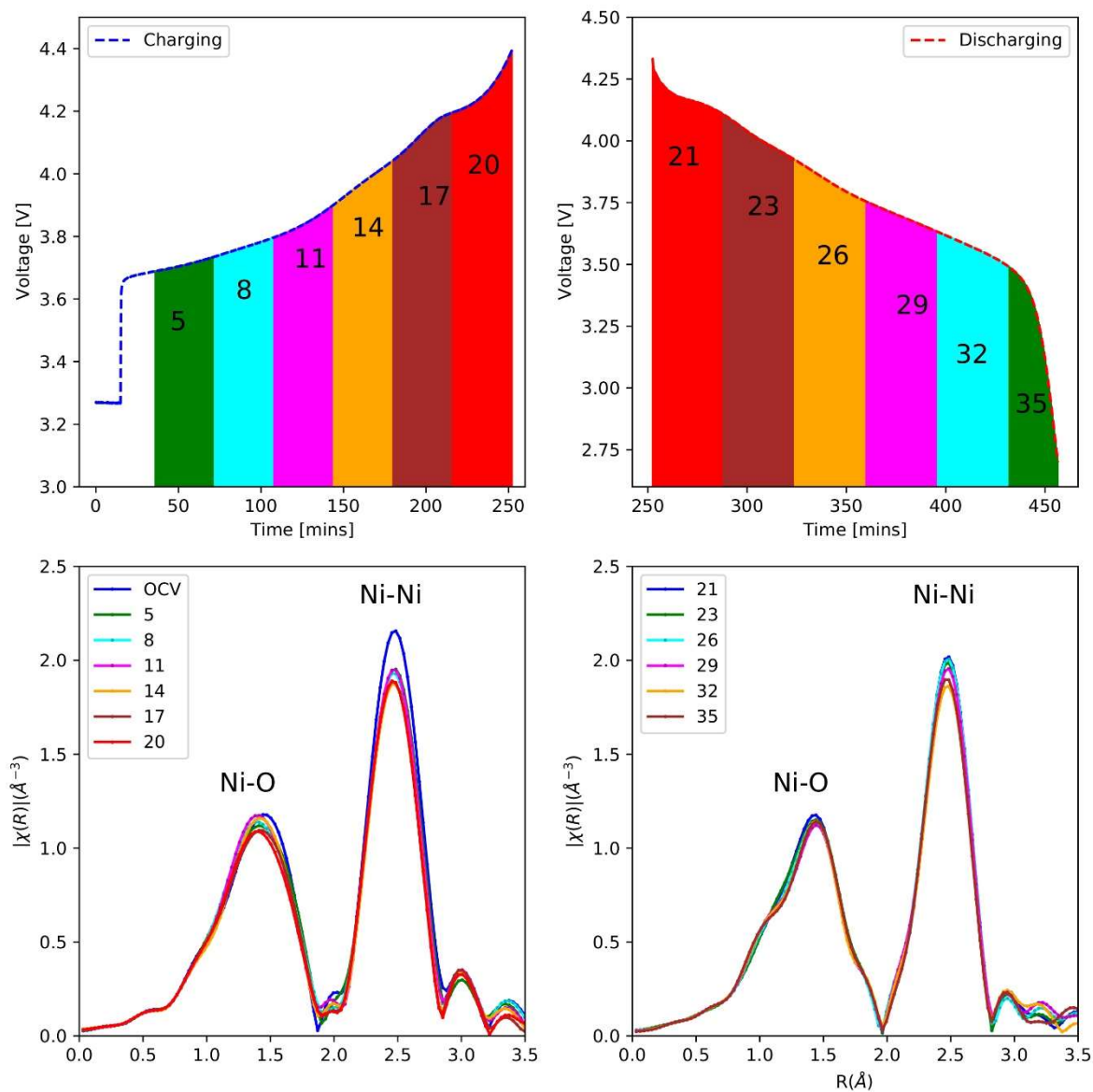


Figure S13. Second-cycle Ni K-edge EXAFS spectra of NCM900505 cathode. Fourier transform of Ni K-edge EXAFS during charging (left) and discharging (right) are shown. In the second cycle, no significant changes in EXAFS are observed.

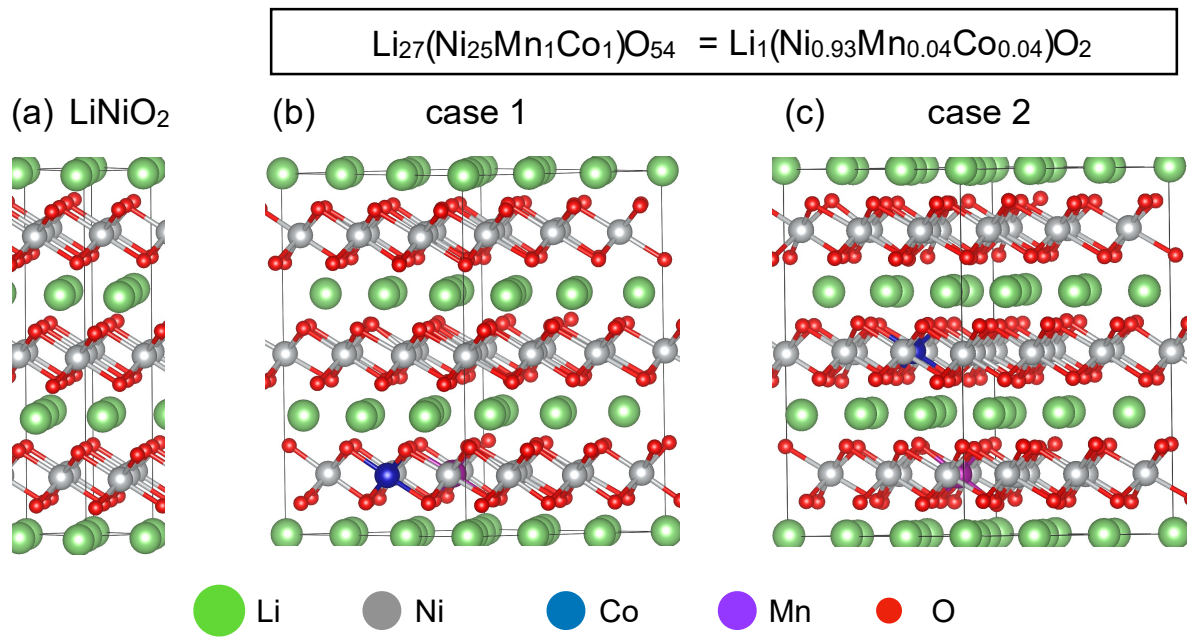
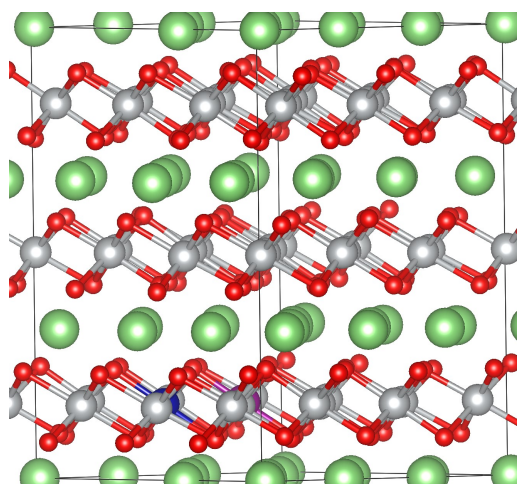


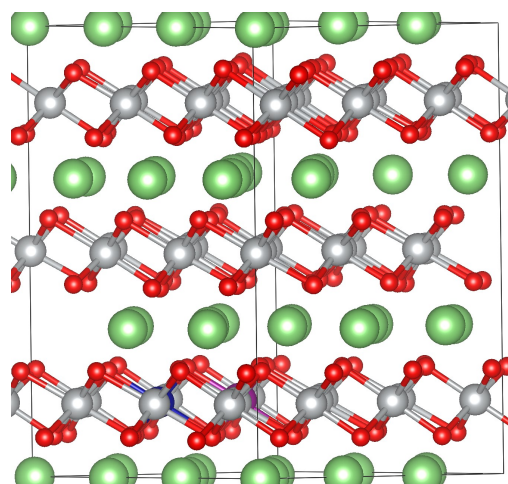
Figure S14. (a) Conventional hexagonal phase (H1) of  $\text{LiNiO}_2$ . (b)-(c) supercells of  $\text{Li}_{27}\text{Ni}_{25}\text{Mn}_1\text{Co}_1\text{O}_{54}$  with different Co and Mn positions.



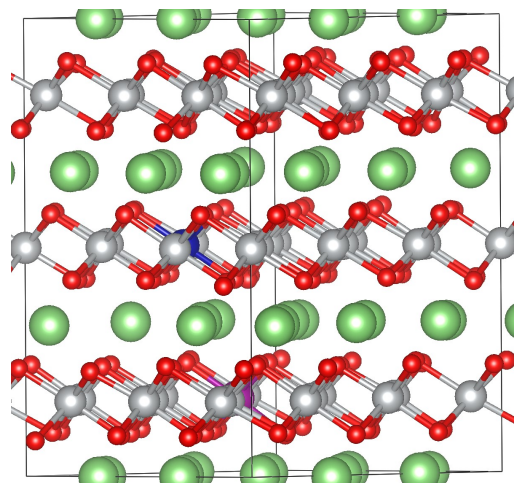
(a) case 1-1



(b) case 1-2



(c) case 2-1



(d) case 2-2

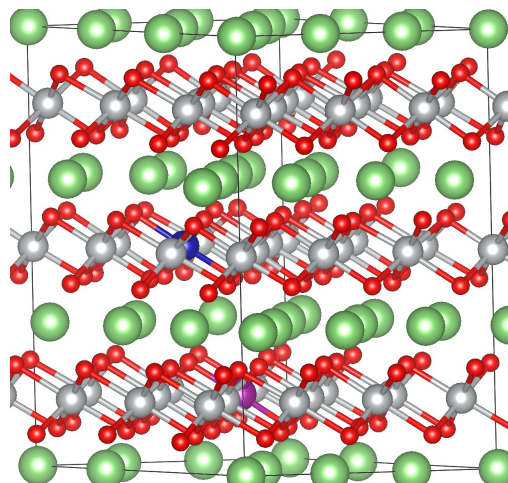


Figure S15 (a)-(d) supercells of  $\text{Li}_{24}\text{Ni}_{25}\text{Mn}_1\text{Co}_1\text{O}_{54}$  with different positions of Co, Mn, and 3 Li-vacancies.

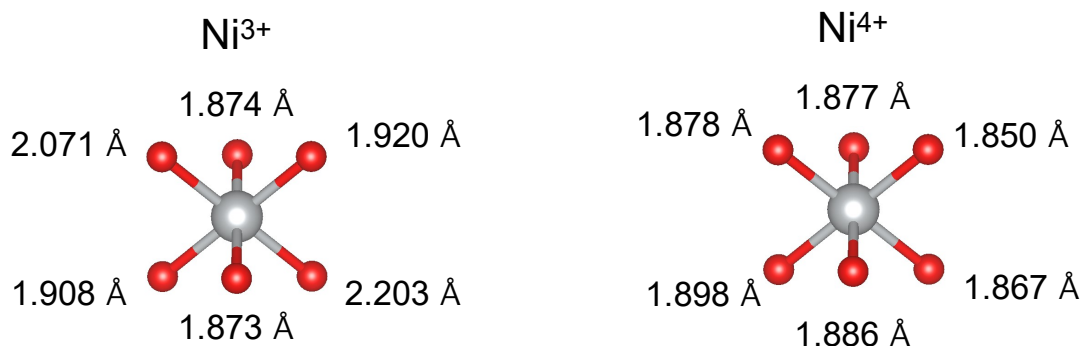


Figure S16. Ni-O bond lengths of (a)  $\text{Ni}^{3+}\text{O}_6$  and (b)  $\text{Ni}^{4+}\text{O}_6$  octahedra.

Table S3. Charge (oxidation) states of Ni ions in the supercell. We consider 2 and 4 different atomic configurations for  $\text{Li}_1(\text{Ni}_{0.93}\text{Mn}_{0.04}\text{Co}_{0.04})\text{O}_2$  and  $\text{Li}_{0.89}(\text{Ni}_{0.93}\text{Mn}_{0.04}\text{Co}_{0.04})\text{O}_2$ , respectively.

case	$\text{Li}_{27}(\text{Ni}_{25}\text{Mn}_1\text{Co}_1)\text{O}_{54}$ = $\text{Li}_1(\text{Ni}_{0.93}\text{Mn}_{0.04}\text{Co}_{0.04})\text{O}_2$	$\text{Li}_{24}(\text{Ni}_{25}\text{Mn}_1\text{Co}_1)\text{O}_{54}$ = $\text{Li}_{0.89}(\text{Ni}_{0.93}\text{Mn}_{0.04}\text{Co}_{0.04})\text{O}_2$
1	$1 \times \text{Ni}^{2+}, 24 \times \text{Ni}^{3+}$	$23 \times \text{Ni}^{3+}, 2 \times \text{Ni}^{4+}$
2	$1 \times \text{Ni}^{2+}, 24 \times \text{Ni}^{3+}$	$23 \times \text{Ni}^{3+}, 2 \times \text{Ni}^{4+}$
3	$2 \times \text{Ni}^{2+}, 24 \times \text{Ni}^{3+}, 1 \times \text{Ni}^{4+}$	$2 \times \text{Ni}^{2+}, 19 \times \text{Ni}^{3+}, 4 \times \text{Ni}^{4+}$
4	$2 \times \text{Ni}^{2+}, 24 \times \text{Ni}^{3+}, 1 \times \text{Ni}^{4+}$	$1 \times \text{Ni}^{2+}, 21 \times \text{Ni}^{3+}, 3 \times \text{Ni}^{4+}$

## References

- 1 K. Heo, J. Lee, Y.-W. Song, M.-Y. Kim, H. Jeong, A. DoCheon, K. Jaekook and J. Lim, *J Electrochem Soc*, 2021, **168**, 010521.
- 2 J. Rodriguez-Carvajal, *Physica B*, 1993, **192**, 55–69.
- 3 G. T. Park, H. H. Ryu, N. Y. Park, C. S. Yoon and Y. K. Sun, *J Power Sources*, 2019, **442**, 227242.
- 4 T. Thien Nguyen, U. H. Kim, C. S. Yoon and Y. K. Sun, *Chemical Engineering Journal*, 2021, **405**, 126887.
- 5 H. H. Ryu, K. J. Park, C. S. Yoon and Y. K. Sun, *Chemistry of Materials*, 2018, **30**, 1155–1163.
- 6 J. J. Rehr and R. C. Albers, *Rev Mod Phys*, 2000, **72**, 621–654.
- 7 B. Ravel and M. Newville, *J Synchrotron Radiat*, 2005, **12**, 537–541.
- 8 A. L. Ankudinov, B. Ravel, J. J. Rehr and S. D. Conradson, *Phys Rev B*, 1998, **58**, 7565–7575.
- 9 P. E. Blöchl, *Phys Rev B*, 1994, **50**, 17953–17979.
- 10 J. P. Perdew, A. Ruzsinszky, G. I. Csonka, O. A. Vydrov, G. E. Scuseria, L. A. Constantin, X. Zhou and K. Burke, *Phys Rev Lett*, 2008, **100**, 136406.
- 11 G. Kresse and J. Hafner, *Phys Rev B*, 1993, **47**, 558–561.
- 12 A. I. Liechtenstein, V. I. Anisimov and J. Zaanen, *Phys Rev B*, 1995, **52**, R5467–R5470.
- 13 A. T. Lee and S. Ismail-Beigi, *Phys Rev B*, 2020, **101**, 144423.
- 14 A. Tkatchenko and M. Scheffler, *Phys Rev Lett*, 2009, **102**, 073005.
- 15 M. Dixit, B. Markovsky, F. Schipper, D. Aurbach and D. T. Major, *Journal of Physical Chemistry C*, 2017, **121**, 22628–22636.